Size, Ligand, and Defect-Dependent Electron-Phonon Coupling in Chalcogenide and Perovskite Nanocrystals and Its Impact on Luminescence Line Widths

Journal Article

Author(s):
Yazdani, Nuri (iD); Volk, Sebastian (iD); Yarema, Olesya (iD); Yarema, Maksym (iD); Wood, Vanessa (iD)

Size, Ligand, and Defect Dependent Electron-Phonon Coupling in Chalcogenide and Perovskite Nanocrystals and its Impact on Luminescence Linewidths

Nuri Yazdani[1]*, Sebastian Volk[1]*, Olesya Yarema[1], Maksym Yarema[1], Vanessa Wood[1]

1. Department of Information Technology and Electrical Engineering, ETH Zurich, CH-8092 Switzerland

Nanocrystals, quantum dots, phonons, electron-phonon coupling, emission linewidth

Abstract

Systematic study of electron-phonon coupling in nanocrystals (NC) via first-principles methods has been limited by the large system sizes presented by the NCs. Here, we present a method to extract electron-phonon coupling strengths from ab initio Molecular Dynamics simulations that is computationally less demanding. We use this method to investigate how electron-phonon coupling strengths depend on NC size, ligands, and defects for the model system of PbS NCs and also demonstrate its general applicability by leveraging the approach to compute electron-phonon coupling strengths in CdSe and $CsPbI_3$ NCs. The strong coupling of phonons to interband transitions in all NCs imposes fundamental limits to emission linewidths. Our results indicate that coupling to localized vibrations stemming from undercoordinated atoms on the surface of the NCs contribute significantly to linewidth broadening, and help to explain the experimentally observed trend that homogenous linewidths decrease with increasing NC size. Finally, we also demonstrate that mild surface defects on the NCs, which do not impact the ground state electronic structure of the NC, can dramatically increase radiative linewidths.
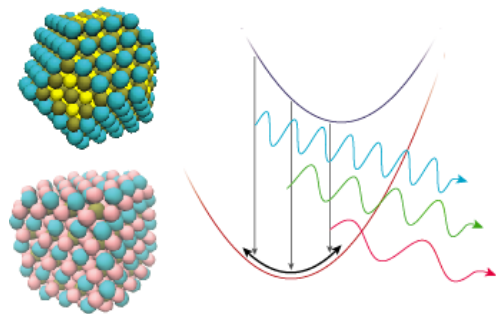
Keywords: nanocrystals, quantum dots, electron-phonon coupling, emission line broadening, lead-halide perovskites

The facile and scalable syntheses of colloidal semiconductor nanocrystals (NCs), combined with the tunability of their optical and electronic properties, and their compatibility with low cost solution processing of devices, render them promising candidates for a variety of optical and optoelectronic applications.[1–5] However, strong electron-phonon coupling (EP-coupling) observed in these systems drives multi-phonon mediated transitions, such as broadening of optical transitions,[6,7] intra-band cooling,[8–10] nonradiative recombination of carriers,[11–13] and charge transfer in solid state ensembles,[14] imposing fundamental limits to the efficiency of applications and devices utilizing NCs.

A good example of this is the photoluminescence (PL) linewidth, a key performance parameter for applications which utilize NCs for their emission. As the synthesis of NCs has improved, the PL linewidths of many NC systems are no longer limited by inhomogeneous broadening of the NC ensemble due, for example, to a NC size distribution. Instead, the PL linewidth is determined by the intrinsic phonon-broadened linewidth of individual NCs (in some cases, amounting to 10% of the emission energy). Linewidths are larger than in bulk samples of the same semiconductor, indicating an enhancement of EP-coupling in NCs, further evidenced by a universal increase in the NC linewidth with decreasing NC size is observed for core-only chalcogenide and perovskite NCs (see **Fig. 1A**).[15–19]

Determining the strengths and origins of EP-coupling through first-principles calculations in NCs can enable the systematic optimization of linewidths, for example, through surface engineering.[20–22] However, computing EP-coupling strengths in NCs presents a unique challenge due to their large size (100s to 10,000s of atoms), and the need to include the complete structural complexity of the NC, including its surface facets and surface-terminating ligands.

3

Within the harmonic approximation, the coupling of a phonon (vibration) with frequency ω to a transition from the state ψ_i to the state ψ_j is given by the dimensionless Huang-Rhys parameter $S_{ij,\omega}$.[23] As shown in **Fig. 1B**, $S_{ij,\omega}$ is related to the shift in the normalized equilibrium atomic coordinates of the atoms ($Q_{i\omega}$ and $Q_{j\omega}$) between states ψ_i and ψ_j in the direction of the vibration.[24,25] Given the set of $\boldsymbol{S}_{ij,\omega}$ for each phonon with frequency ω which couples to the transition of interest, one can compute the temperature dependent rates of both radiative and non-radiative transitions between ψ_i and ψ_j.[26]

Various classes of electron-phonon coupling to inter- and intra-band transitions in chalcogenide and perovskite NCs have been demonstrated, including Frohlich type coupling of longitudinal-optical (LO) phonons,[6,27–30] and deformation-potential type coupling to confined acoustic modes[6,27,31–33] and localized vibrations on the NC surface resulting from a modified chemical environment due to undercoordination and ligand binding.[13,20]

Unfortunately, without a priori knowledge of which phonons/vibrations exist in the NC and which modes couple to the transition of interest, all $3N_A$-6 of the $\boldsymbol{S}_{ij,\omega}$ must be calculated, where N_A is the number of atoms in the system. Utilizing density functional theory (DFT) based 'atomic-displacement/frozen-phonon' approaches[34,35] to estimate the $\boldsymbol{S}_{ij,\omega}$ therefore requires $3N_A$-6 independent self-consistent energy calculations. In the best case, the computation time for each self-consistent energy calculation scales with N_A, and the overall time to estimate the set $\boldsymbol{S}_{ij,\omega}$ goes as $\sim 3N_A^2$. Such approaches are feasible for molecules and bulk materials with relatively small N_A (for bulk calculations, N_A is the number of atoms in the supercell used for the calculation). However, the large systems sizes presented by the NCs, with N_A in the range of hundreds to tens of thousands of atoms (**Fig. 1C**), limit the applicability of standard ab-initio calculation schemes often employed.

Here, we present an efficient and conceptually facile method to obtain complete spectral representations of EP-coupling strengths, $S_{ij}(\omega_k)$, from *ab-initio* Molecular Dynamics (AIMD) simulations. The method scales linearly with system size, enabling the study of NCs with sizes relevant for optoelectronic devices. We show that this method can be applied to investigate the impact of NC size and ligands on electron-phonon coupling strengths in lead-sulfide (PbS) NCs, confirming experimentally observed trends. We show that atomistic surface defects, which have negligible impact on the electronic structure of the NC, can lead to a dramatic increase in the EP-coupling strengths. Finally, we confirm the general applicability of the approach by computing EP-coupling strengths in cadmium-selenide (CdSe)[36] and cesium-lead-iodide (CsPbI₃) NCs,[37] the results of which show good agreement to previous spectroscopic studies.
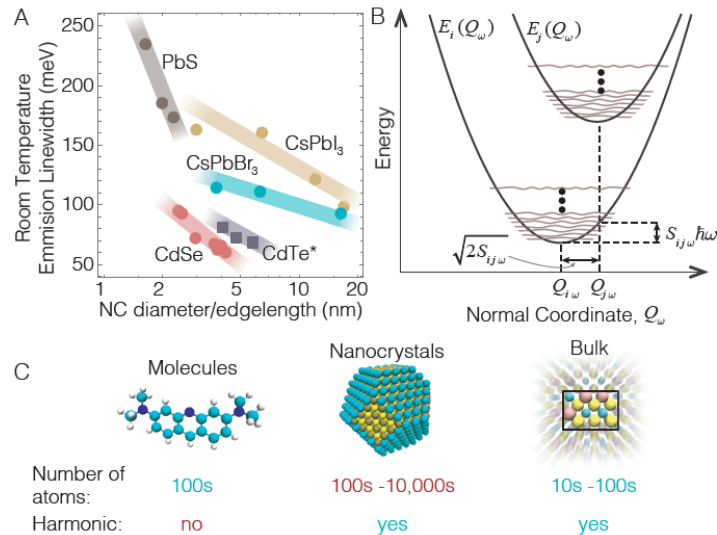
Figure 1. Electron phonon coupling in semiconductor nanocrystals. *(A) Plot of the photoluminescence (PL) linewidth of various semiconductor NCs as a function of size, taken from literature. Measurements on PbS,[15] CdSe,[17], and CsPbX₃,[19] are for single NCs while the measurements for CdTe[18] were performed on an ensemble. (B) Configuration diagram for states ψ_i and ψ_j along the axis of a particular phonon with frequency ω. The shifted harmonic oscillator atomic wavefunctions for each state are shown as the grey lines. The EP-coupling of the phonon with frequency ω to transitions between ψ_i and ψ_j is related to the shift $Q_{i\omega} - Q_{j\omega}$. (C) Atomic*

models of a small molecule, a NC, and an unit cell of a bulk semiconductor, indicating typical system sizes.

AIMD is a powerful method for investigating dynamical processes at the atomic scale,[38–40] from which one can simultaneously obtain the atomic trajectories and the adiabatic ground-state electronic structure of the system being simulated. From the atomic trajectories, we can directly compute the phonon density of states of the NC, $g(\omega)$, along with the partial density of states for each atom in the NC, $g_i(\omega)$ (see **Supporting Information Note 1**). The $g(\omega)$ extracted from AIMD has been shown to be in good agreement with the $g(\omega)$ of NCs experimentally measured using inelastic neutron- and x-ray scattering.[13,41] The EP-coupling strengths can then be computed from the time-dependent adiabatic electronic structure.

In the AIMD, each degree of freedom (or vibrational mode) has an average energy of k_BT and a time-dependent normal coordinate:

$$Q_\omega(t) = \sqrt{\frac{2k_BT}{\hbar\omega}}e^{i\omega t+\phi} + Q_{0\omega}, (1)$$

where $Q_{0\omega}$ is the equilibrium normal coordinate in the ground state. The time-dependent energy of the transition from any two electronic states in the system, $\psi_i \to \psi_j$, is then given by

$$E_j(t) - E_i(t) = \left(E_j - E_i\right) + \sum_\omega \left[\frac{1}{2}\hbar\omega\left(Q_\omega(t) - Q_{j\omega}\right)^2 - \frac{1}{2}\hbar\omega(Q_\omega(t) - Q_{i\omega})^2\right],$$

$$= \left(E_j - E_i\right) + \sum_\omega\left(\sqrt{S_{0i,\omega}S_{ij,\omega}} + \sqrt{S_{0j,\omega}S_{ij,\omega}}\right)\hbar\omega + \sum_\omega\sqrt{4S_{ij,\omega}\hbar\omega k_BT}e^{i\omega t+\phi}. (2)$$

Referring back to the schematic in **Figure 1B**, the first term is the energy difference between state E_i and E_j (the bottom of the two parabolas); the 2nd term is the shift in energy of the transition between states i and j due to the normal coordinates of one or both states being shifted away from $Q_{0\omega}$ (i.e., the Stokes shift of the transition); and the third term is the time-dependence of the energy

due to the motion of the atomic coordinates at a given temperature T (along by the adiabatic energy surfaces, i.e., the parabolas in **Figure 1B**). Only the third term is time dependent, and we can therefore extract a spectral representation of the coupling strengths $S_{ij}(\omega_k)$ via a Fourier transform, $\mathcal{F}\{\dots\}$, of the time dependent energies

$$S_{ij}(\omega_k) = \left|\mathcal{F}\{E_j(t) - E_i(t)\}\right|^2/4\hbar\omega k_B T. \ (3)$$

For a finite system (such as a NC) Eq. 3 allows, from a single AIMD simulation, the simultaneous calculation of $S_{ij}(\omega_k)$ for all transitions and over the entire frequency range of vibrational modes from a single AIMD simulation of the system. The spectral resolution of $S_{ij}(\omega_k)$ is determined by the number of time steps of the AIMD run, and the extracted $S_{ij}(\omega_k)$ at a particular ω_k is the sum of the $S_{ij\omega}$ over all modes within the frequency range $(\omega_k - 1/2\Delta\omega, \omega_k + 1/2\Delta\omega)$ where $\Delta\omega = \omega_k - \omega_{k-1}$.

The emission linewidth can be determined from the $S_{E_g}(\omega_k)$, the EP-coupling to the band-gap. In the strong coupling limit,[26] $\sum_k S_{E_g}(\omega_k) \gg 1$, the emission will have an approximate Gaussian lineshape, with a temperature-dependent linewidth

$$L(T) = 2.355 \cdot \sqrt{\sum_k S_{E_g}(\omega_k)(\hbar\omega_k)^2(2n(\omega_k, T) + 1)}, \quad n(\omega_k, T) = \left(e^{\hbar\omega_k/k_B T} - 1\right)^{-1}. \ (4)$$

At high temperatures $(k_B T > \omega_{max})$, we can invoke the semiclassical approximation with a linewidth given by[24,26]

$$L_{SC}(T) = 2.355\sqrt{2\Lambda k_B T}, \ (5)$$

where Λ is the reorganization energy of the transition:

$$\Lambda = \sum_k S_{ij}(\omega_k)\hbar\omega_k. \ (6)$$

This approach is best used with AIMD simulations performed at low temperatures. This ensures that: (i) there is negligible anharmonic motion, which that may be present at elevated temperatures, such that Eq. 2 holds, and (ii) the time dependent energies of both states can be uniquely determined such that there are no avoided crossings of the adiabatic levels. Similarly, care must be taken if the transition under question is degenerate. Further discussion can be found in **Supporting Information Note 2**. We note that as this AIMD based approach ignores electron-hole interactions. While this should be a reasonable approximation in the limit of strong quantum confinement of carriers in a NC, it can be poor in the case of higher dimensional systems (1D to bulk), where this interaction is required to capture excitonic states.

We first apply this method to calculate EP-coupling strength in PbS NCs and its impact on the linewidth. We choose PbS NCs as a model system due to the extensive previous work characterizing phonons, EP-coupling, and phonon-mediated transitions in lead-chalcogenide NCs.[13–15,20,41–45] We begin by considering a PbS NC of diameter d =2.48 nm with chlorine (Cl) ligands and utilize the approach above to calculate its expected emission linewidth (see **Fig. 2A-B**). AIMD simulations of the NC are performed as described in the **Methods** at a temperature of 10 K. The time-dependent adiabatic electronic structure of the NC is shown in **Figure 2C**, from which we calculate the time dependent band-gap, $E_G(t)$ (**Figure 2D**).

Using Eq. 3, we calculate the EP-coupling to the band-gap, $S_{E_g}(\omega_k)$ for the 2.48 nm diameter NC, and plot the result in **Figure 2E**. We identify 4 groups of modes (with energies $\hbar\omega \sim 3.5$ meV, 8.0 meV, 17.0 meV, and 24.5 meV) that couple to the transition.

Since we are in strong coupling limit,[26] $\sum_k S_{E_g}(\omega_k) \gg 1$, we use the semiclassical expression in Eq. (5), to determine the linewidth as a function of temperature (**Figure 2F**), and find a room

temperature linewidth of 93 meV. We also plot the linewidth computed directly from the adiabatic electronic structure:

$$L_{AIMD}(T) = 2.355 \sqrt{\text{Var}\big(E_g(t,T)\big)}, \quad (7)$$

for AIMD simulations run at temperatures from 10 K to 300 K (blue dots). While the computed forces in AIMD are quantum, the thermal occupation of modes is classical. The linewidths extracted directly from AIMD, Eq. 7, therefore show excellent agreement to the semiclassical result computed with Eq. 5 using the $S_{E_g}(\omega_k)$ extracted from the 10 K AIMD. By calculating the linewidth with the full expression in Eq. 4 (the solid line in **Figure 2F**), one appropriately accounts for finite broadening due to phonon sidebands at low-temperatures (a result of 0-point motion). Overall, the temperature dependence indicates that for this PbS/Cl NC, there is no appreciable anharmonic contribution to the linewidth at elevated temperatures.
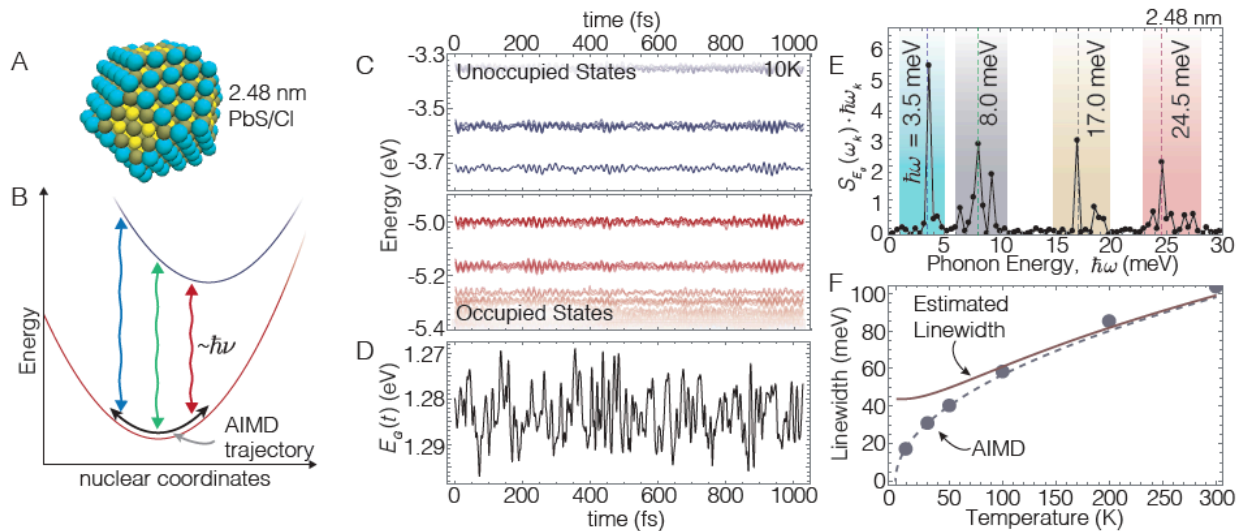
Figure 2. Extracting EP-Coupling from AIMD simulations. *(A) 2.48 diameter, Cl-terminated PbS NC. (B) Schematic showing that in the case of strong EP-coupling large fluctuations are observed in the bandgap of the NC and the emitted energy of the light, hv. (C) Adiabatic electronic structure and (D) time-dependence of the bandgap energy. (E) EP-coupling strengths for transitions across the bandgap calculated with Eq. 3, and scaled by the phonon energy ℏω*

indicate coupling to four sets of modes. (F) The temperature-dependent linewidths calculated by eq. 4 using the extracted $S_{E_g}(\omega_k)$ (solid line), the semiclassical approximation (eq. 5) (dashed), and computed directly from AIMD simulations performed at various temperatures (eq. 7) (points) are shown.

We apply our approach to determine the impact of NC size and surface termination on the EP-coupling strengths. We performed AIMD at 10 K on $d = 1.8$, 2.48, 2.84, and 3.60 nm PbS/Cl NCs, and use Eq. 3 to compute the EP-coupling strengths to transitions across the bandgap, $S_{E_g}(\omega_k)$. To highlight the trends with size, we reduce the extracted $S_{E_g}(\omega_k)$ into a four-mode model, by summing the $S_{E_g}(\omega_k)$ over the shaded regions in **Fig. 2E**. For example, the coupling to the low energy modes is renormalized to a single mode with an energy 3.5 meV:

$$\tilde{S}_{E_g}(3.5 \text{ meV}) \equiv \frac{1}{3.5} \sum_{\substack{\omega_k \geq 1 \text{ meV}}}^{\omega_k \leq 6 \text{ meV}} S_{E_g}(\omega_k) \cdot \hbar\omega_k \quad (8)$$

We plot the extracted $\tilde{S}_{E_g}(\omega_k)$ as a function of NC size in **Fig. 3B**, from which it is apparent that the coupling to all four effective modes decreases as the size of the NC increases. This is consistent with the size dependence of the linewidth observed in experiment.[15]

As we show in **Supporting Information Note 3**, the energies of the effective modes that couple with $\hbar\omega \sim 3.5$ meV, 17.0 meV, and 24.5 meV, are independent of NC size. This is consistent with previous reports that, in PbS NCs, localized vibrations on the surface of the NCs couple to inter- and intra-band transitions. As the strength of the coupling will scale with the spatial overlap of the exciton wavefunctions with the surface vibrations, a decrease in the coupling of these modes with increasing size is also as expected.[13,20] On the other hand, the mode with $\hbar\omega \sim 8$ meV shows a monotonic decrease in energy with an increase in the nanocrystal diameter, with $\hbar\omega \sim d^{-0.7}$. The energetic scale of this mode (from ~6 meV to ~9 meV), its scaling with NC size (reduced in these

small NCs relative to the d^{-1} expected for an elastic continuum[22]), and the scaling of its coupling strength, point toward coupling of a confined longitudinal acoustic mode, or spheroidal Lamb mode, as previously deduced from Raman measurements.[27]
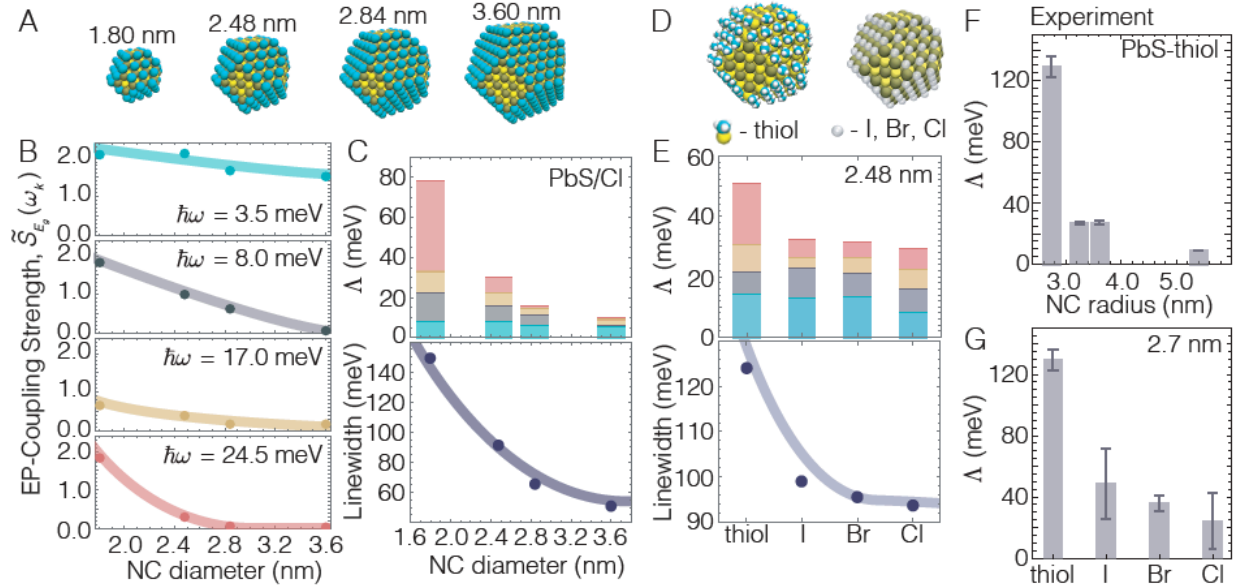

Figure 3. Size and ligand dependence of EP-coupling. *(A) Atomistic models of the 4 PbS/Cl NC sizes considered here. (B) EP-coupling strengths, $\tilde{S}_{E_g}(\omega_k)$ and (C) reorganization energies, Λ, and room temperature linewidths for the transition across the bandgap. The plots of Λ are decomposed into the contributions to Λ from each of the four modes, using the color scheme in (B). (D) Atomistic models for 1.24 nm NCs with methanethiol ligands and halide ligands. (E) Extracted Λ and linewidths. In (B), (C), and (E), the semi-transparent lines are guides for the eye. Experimentally measured reorganization energies, Λ, as a function of NC size for (F) thiol-terminated PbS and (G) 2.7 nm diameter PbS NCs with thiol and different halide passivations.*

We also investigate the impact of the ligands and calculate the EP-coupling on 2.48 nm NCs with thiol ligands (here methanethiol) and halide ligands (**Fig. 3D**). In **Fig. 3E** we plot the reorganization energies and expected room-temperature linewidths for each ligand. We find a decrease in the EP-coupling and linewidths going from thiol, to iodide, to bromide, to chlorine surface termination. The linewidth for the Cl-terminated NC relative to the thiol-terminated NC is reduced by ~25%, consistent with previous findings.[20]

11

These observations trends are of decreased EP-coupling with increasing NC size and decreased coupling with halide surface treatment for the transition across the band gap are confirmed experimentally using temperature dependent Fourier-transform-photocurrent-spectroscopy measurements on PbS NC thin films (**Supporting Information Note 4)**. In **Fig. 3F** we plot the estimated reorganization energy, Λ, extracted from experiment, as a function of NC size for PbS-thiol NCs, which confirms a decrease in the EP-coupling with increasing NC size. We also confirm the trend predicted by the calculations for thiol and halide ligands, as shown in **Fig. 3G**.

While the experimentally measured trends match the predictions from the calculations, we find that the experimentally extracted EP-couplings are larger than those calculated. Similarly, the linewidths predicted from the calculations (**Fig. 3C,E**) are notably smaller than those previously measured on single PbS NCs using photon correlation Fourier spectroscopy.[15] We investigate whether small structural defects on the surface of NCs, such as missing or surplus cations, anions, or ligands, could be responsible for the larger than expected EP-coupling strengths and linewidths. To do so, we construct two 2.48 nm PbS/Cl NCs with mild structural surface defects (**Fig. 4A**): one NC with a single missing Cl ligand and one NC with a single Pb-Cl pair missing.

We plot the electronic structure of the defect-free NC (with full octahedral symmetry, labelled 'symmetric') along with the electronic structure of the two defected NCs in **Fig. 4B**. Beyond a moderate lifting of the degeneracies of the states (< 20 meV for the 6 fold-degenerate, highest occupied electronic states), the electronic structure off all three NCs is essentially identical with no sign of mid-gap state formation in the NCs with structural defects. In **Fig. 4C**, we plot the wavefunctions of the highest occupied and lowest unoccupied states, which look essentially identical for all three NCs, with no sign of localization of the exciton at or around the defects. We therefore conclude that these defects negligibly alter the ground state electronic structure.
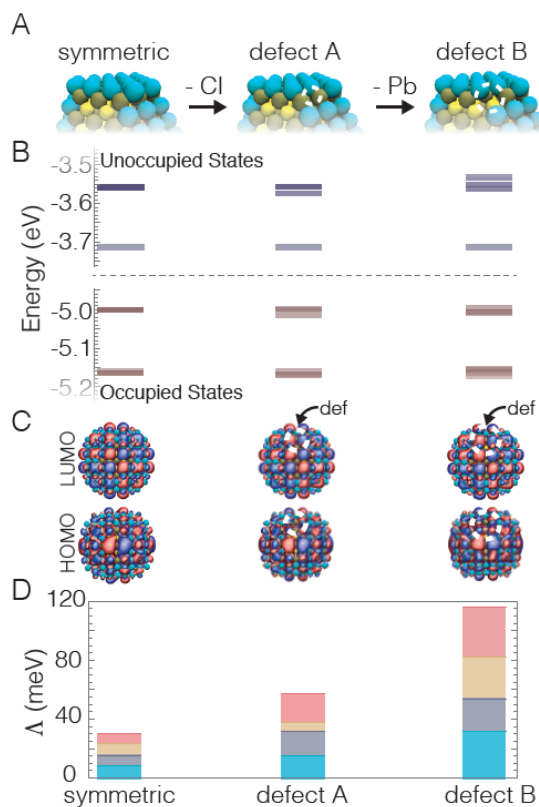
Figure 4. Impact of surface defects on EP-coupling. *(A) Atomistic models of a 'symmetric' NC with full octahedral symmetry and defected PbS/Cl NCs. Plots of the electronic structure of the NCs about the bandgap are given in (B) and contour plots of the wavefunctions of the highest occupied state and lowest unoccupied state are shown in (C). Computed reorganization energies, Λ, for each NC, with the bars decomposed into the contribution from coupling to $\hbar\omega = 3.5$ meV (blue), 8.0 meV (purple), 17.0 meV (yellow) and 24.5 meV (red) modes.*

In **Fig. 4D**, we plot the reorganization energy Λ computed for the three NCs, where we find a dramatic increase in the EP-coupling strengths for the NCs with defect. For the Pb-Cl pair defect, this increase is four-fold compared to the defect free NC, corresponding to a two-fold increase in the expected room temperature linewidth. This is a result of an significant decrease in the coordination of surface atoms surrounding the defects, leading to further localization of vibrational modes to the NC surface and an increase in EP-coupling.[20] We note that, in addition, defects could potentially introduce anharmonic vibrations, further broadening the linewidth. These findings highlight how structural defects on the surface of the NC can strongly modify EP-coupling strengths without inducing any noticeable change in the ground state electronic structure.

Finally, we demonstrate the generality of our AIMD based approach by also calculating EP-coupling and linewidths for CdSe and CsPbI$_3$ NCs. We first consider a 1.4 nm zincblende CdSe NC with Cl surface termination.[46,47] In **Fig. 5A**, we plot EP-coupling strengths to transitions across the bandgap, $S_{E_g}(\omega_k)$, along with the phonon density of states of the CdSe NC, $g(\omega)$, and the partial density of states for the Cd, Se, and Cl atoms, $g_i(\omega)$. We find three main groups of modes which couple to the lowest energy transition, with energies $\hbar\omega \sim 5$ meV, 16 meV, and 26 meV. A size-independent coupling to the longitudinal optical (LO) phonon mode in CdSe ($\hbar\omega \sim 25.5$ meV) with $S_{E_g}(25.5 \text{ meV}) \sim 0.1$ to 0.5 has been extensively reported in the literature,[29,36,48–52] and is in good agreement with our finding of $S_{E_g}(26 \text{ meV}) = 0.28$. In addition, size-dependent coupling of $\hbar\omega \sim 3\text{-}6$ meV[53,54] and ~15 meV[54] modes in core only CdSe NCs have been reported in literature, which we see in our simulated results. The predicted room-temperature linewidth from our results is ~134 meV, which closely matches the expected linewidth extrapolated from the size dependence of the linewidth measured previously (see **Fig. 1A**).[17]

In **Fig. 5B** we show the results for a CsPbI$_3$ NC with 2.4 nm edgelength. We first note a coupling to modes at the LO phonon energy (~13.5 meV) with $S_{E_g}(13.5 \text{ meV}) = 0.4$, in good agreement with LO phonon coupling strengths measured in CsPbBr$_3$[55] and FAPbBr$_3$[6] NCs. We further observe coupling to broad sets of modes centered about $\hbar\omega \sim 1.5$ meV and 5 meV. Such coupling to both low and intermediate phonons has been demonstrated in single formamidinium-lead-bromide FAPbBr3 NCs,[6] and, accounting for the red-shift of phonon frequencies in CsPbI$_3$ relative to FAPbBr$_3$, the ranges of modes found from our calculations match those measured. Our calculations predict a room-temperature linewidth of ~112 meV, notably smaller than the estimate (~175 meV) predicted by the size dependence from experiment.[19] This may come as a result of (i)

structural 'defects', as discussed above (**Fig. 4**), such as missing Cs atoms and Pb-I pairs, or inhomogeneous ligand coverage on the surface of the NCs,[56] or (ii) anharmonic contributions to the linewidth at elevated temperatures.
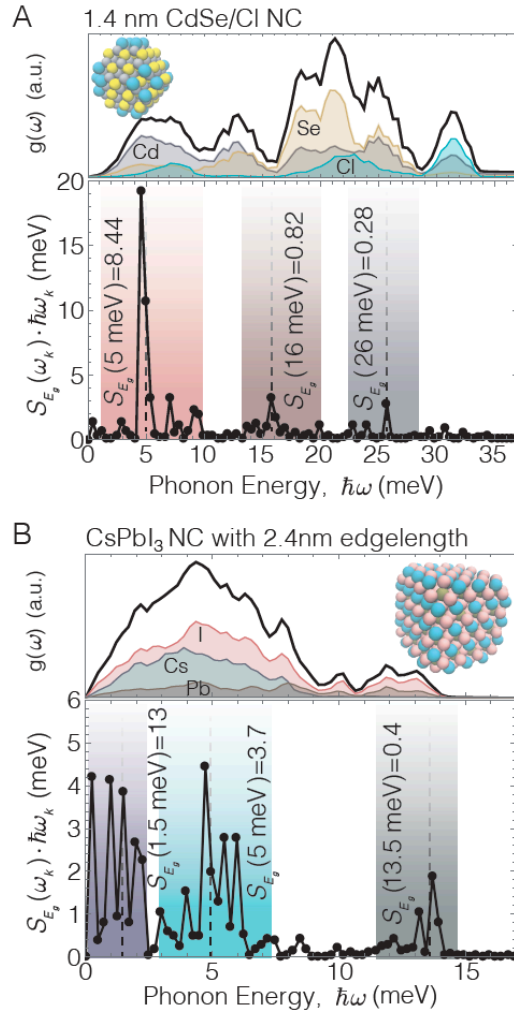
Figure 5. EP-coupling in CdSe and CsPbI₃ NCs. *Plot of the phonon density of states (black line), partial density of states for each atom type, and calculated EP-coupling for a (A) CdSe/Cl NC and (B) CsPbI₃ NC.*

In summary, we have introduced a new method to extract EP-coupling strengths from AIMD simulations, a method which enables the study of EP-phonon coupling in large system sizes. We used this method to gain further insight into EP-coupling in PbS NCs, demonstrating the size and

ligand dependence of the coupling to the lowest energy transition, which we checked against experiment. We found strong enhancement of EP-coupling in NCs resulting from structural surface defects, which do not generate electronic defects, shedding light on their impact of the broadening of optical transitions. Finally, we have provided initial results for EP-coupling in CdSe and $CsPbI_3$ NCs, which indicate that, similar to PbS, the emission linewidths in these NCs are limited by coupling to low energy phonons, as opposed to LO phonon coupling. Future calculations on these systems should be able to pinpoint the origin of this coupling, as well as provide means to mitigate their impact on the emission linewidth.

Methods

PbS and CdSe NCs are constructed as reported previously.[20,46] The cubic $CsPbI_3$ NCs are cut directly from bulk $CsPbI_3$ in the cubic phase, with the corner Cs atoms removed. For all NCs, we fully geometry relax all atoms. For the $CsPbI_3$ NCs we find that the atomic structure of the NCs after full geometry-relaxation is independent of the starting bulk phase (i.e. orthorhombic or cubic).[41,57] In order to maintain overall charge balance of the NCs, we add/remove additional electrons to the NCs. As we have previously discussed, such charges could be given through bonding with surface ligands and/or counter ions in solution. Utilizing this approach, as opposed to the removal of ligands/cations-ligand-pairs/Cs-atoms, we maintain the overall symmetry of the NCs, allowing more systematic comparisons between different NCs (size, ligands etc.), without the addition of any stochastic effects.

All geometry optimization, electronic structure calculations, and ab initio molecular dynamics simulations (AIMD) were performed with the CP2K program suite, using the quickstep module.[58] 300 Ry plane-wave cutoff were used for a dual basis of localized Gaussians and plane-waves, used for all calculations.[59] Goedecker–Teter–Hutter pseudopotentials[60] for core electrons, and the

Perdew–Burke–Ernzerhof (PBE) exchange correlation functional were employed, with an enforced Self-Consistent Field convergence to 10^{-8}. Cubic unit cells were used with edgelengths always at least 1.5 nm larger than the widest axis of the NCs.

We perform AIMD within the canonical ensemble using a CSVR thermostat,[61] with AIMD time steps of 10 fs. For thermalization, calibration, and equilibration of the total energy and temperature, 3 ps of the AIMD are run with the time constant of the thermostat set to 15 fs. This is followed by 11+ ps run of the AIMD with the time constant set to 1ps. The first 4 ps of the AIMD are excluded from the calculations of EP-coupling and phonon density of states.

ASSOCIATED CONTENT

Supporting Information.

The Supporting Information is available free of charge on the ACS Publications website at DOI: https://pubs.acs.org/doi/10.1021/acsphotonics.XXXXXXX.

Discussions on Extracting Phonon Density of States, Impact of Degenerate Transitions, and FTPS Measurements (PDF)

Corresponding Author

*Correspondence to: vwood@ethz.ch
Author Contributions

NY and VW conceived the study. NY developed theory, performed calculations, and analyzed results. MY and OY synthesized materials. SV prepared samples and performed FTPS measurements. SV and NY analyzed experimental data. NY and VW wrote the manuscript with input from all authors.

REFERENCES

(1)   Lim, J.; Park, Y.-S.; Klimov, V. I. Optical Gain in Colloidal Quantum Dots Achieved with Direct-Current Electrical Pumping. *Nat. Mater.* **2017**, *17* (1), 42–49.

(2)   Yakunin, S.; Protesescu, L.; Krieg, F.; Bodnarchuk, M. I.; Nedelcu, G.; Humer, M.; De Luca, G.; Fiebig, M.; Heiss, W.; Kovalenko, M. V. Low-Threshold Amplified Spontaneous Emission and Lasing from Colloidal Nanocrystals of Caesium Lead Halide Perovskites. *Nat. Commun.* **2015**, *6* (1), 8056.

(3)   Gong, X.; Yang, Z.; Walters, G.; Comin, R.; Ning, Z.; Beauregard, E.; Adinolfi, V.; Voznyy, O.; Sargent, E. H. Highly Efficient Quantum Dot Near-Infrared Light-Emitting Diodes. *Nat. Photonics* **2016**, *10* (4), 253–257.

(4)   Ackerman, M. M.; Tang, X.; Guyot-Sionnest, P. Fast and Sensitive Colloidal Quantum Dot Mid-Wave Infrared Photodetectors. *ACS Nano* **2018**, *12* (7), 7264–7271.

(5)   Swarnkar, A.; Marshall, A. R.; Sanehira, E. M.; Chernomordik, B. D.; Moore, D. T.; Christians, J. A.; Chakrabarti, T.; Luther, J. M. Quantum Dot-Induced Phase Stabilization of -CsPbI3 Perovskite for High-Efficiency Photovoltaics. *Science (80-.).* **2016**, *354* (6308), 92–95.

(6)   Fu, M.; Tamarat, P.; Trebbia, J.-B.; Bodnarchuk, M. I.; Kovalenko, M. V; Even, J.; Lounis, B. Unraveling Exciton–Phonon Coupling in Individual FAPbI3 Nanocrystals Emitting near-Infrared Single Photons. *Nat. Commun.* **2018**, *9* (1), 3318.

(7)   Liu, A.; Almeida, D. B.; Bae, W. K.; Padilha, L. A.; Cundiff, S. T. Non-Markovian Exciton-Phonon Interactions in Core-Shell Colloidal Quantum Dots at Femtosecond Timescales. *Phys. Rev. Lett.* **2019**, *123* (5), 057403.

(8)   Kilina, S. V.; Kilin, D. S.; Prezhdo, O. V. Breaking the Phonon Bottleneck in PbSe and CdSe Quantum Dots: Time-Domain Density Functional Theory of Charge Carrier Relaxation. *ACS Nano* **2009**, *3* (1), 93–99.

(9)   Diroll, B. T.; Schaller, R. D. Intraband Cooling in All-Inorganic and Hybrid Organic–Inorganic Perovskite Nanocrystals. *Adv. Funct. Mater.* **2019**, *29* (37), 1901725.

(10)   Schaller, R. D.; Pietryga, J. M.; Goupalov, S. V.; Petruska, M. A.; Ivanov, S. A.; Klimov, V. I. Breaking the Phonon Bottleneck in Semiconductor Nanocrystals via Multiphonon Emission Induced by Intrinsic Nonadiabatic Interactions. *Phys. Rev. Lett.* **2005**, *95* (19), 1–4.

(11)   Shu, Y.; Fales, B. S.; Peng, W.-T.; Levine, B. G. Understanding Nonradiative Recombination through Defect-Induced Conical Intersections. *J. Phys. Chem. Lett.* **2017**, *8* (17), 4091–4099.

(12)   Shu, Y.; Fales, B. S.; Levine, B. G. Defect-Induced Conical Intersections Promote Nonradiative Recombination. *Nano Lett.* **2015**, *15* (9), 6247–6253.

(13)   Bozyigit, D.; Yazdani, N.; Yarema, M.; Yarema, O.; Lin, W. M. M.; Volk, S.;
        Vuttivorakulchai, K.; Luisier, M.; Juranyi, F.; Wood, V. Soft Surfaces of Nanomaterials
        Enable Strong Phonon Interactions. *Nature* **2016**, *531* (7596), 618–622.

(14)   Yazdani, N.; Andermatt, S.; Yarema, M.; Farto, V.; Bani-Hashemian, M. H.; Volk, S.; Lin,
        W.; Yarema, O.; Luisier, M.; Wood, V. Charge Transport in Semiconductors Assembled
        from Nanocrystals. **2019**, arXiv:1909.09739. arXiv.org e-Print archive.

(15)   Caram, J. R.; Bertram, S. N.; Utzat, H.; Hess, W. R.; Carr, J. A.; Bischof, T. S.; Beyler, A.
        P.; Wilson, M. W. B.; Bawendi, M. G. PbS Nanocrystal Emission Is Governed by Multiple
        Emissive States. *Nano Lett.* **2016**, *16* (10), 6070–6077.

(16)   Campos, M. P.; Hendricks, M. P.; Beecher, A. N.; Walravens, W.; Swain, R. A.; Cleveland,
        G. T.; Hens, Z.; Sfeir, M. Y.; Owen, J. S. A Library of Selenourea Precursors to PbSe
        Nanocrystals with Size Distributions near the Homogeneous Limit. *J. Am. Chem. Soc.* **2017**,
        139 (6), 2296–2305.

(17)   Cui, J.; Beyler, A. P.; Coropceanu, I.; Cleary, L.; Avila, T. R.; Chen, Y.; Cordero, J. M.;
        Heathcote, S. L.; Harris, D. K.; Chen, O.; et al. Evolution of the Single-Nanocrystal
        Photoluminescence Linewidth with Size and Shell: Implications for Exciton-Phonon
        Coupling and the Optimization of Spectral Linewidths. *Nano Lett.* **2016**, *16* (1), 289–296.

(18)   Morello, G.; De Giorgi, M.; Kudera, S.; Manna, L.; Cingolani, R.; Anni, M. Temperature
        and Size Dependence of Nonradiative Relaxation and Exciton−Phonon Coupling in
        Colloidal CdTe Quantum Dots. *J. Phys. Chem. C* **2007**, *111* (16), 5846–5849.

(19)   Utzat, H.; Shulenberger, K. E.; Achorn, O. B.; Nasilowski, M.; Sinclair, T. S.; Bawendi, M.

G. Probing Linewidths and Biexciton Quantum Yields of Single Cesium Lead Halide Nanocrystals in Solution. *Nano Lett.* **2017**, *17* (11), 6838–6846.

(20) Yazdani, N.; Bozyigit, D.; Vuttivorakulchai, K.; Luisier, M.; Infante, I.; Wood, V. Tuning Electron–Phonon Interactions in Nanocrystals through Surface Termination. *Nano Lett.* **2018**, *18* (4), 2233–2242.

(21) Park, Y.-S.; Lim, J.; Klimov, V. I. Asymmetrically Strained Quantum Dots with Non-Fluctuating Single-Dot Emission Spectra and Subthermal Room-Temperature Linewidths. *Nat. Mater.* **2019**, *18* (3), 249–255.

(22) Mork, A. J.; Lee, E. M. Y.; Dahod, N. S.; Willard, A. P.; Tisdale, W. A. Modulation of Low-Frequency Acoustic Vibrations in Semiconductor Nanocrystals through Choice of Surface Ligand. *J. Phys. Chem. Lett.* **2016**, *7* (20), 4213–4216.

(23) Huang, K.; Rhys, A. Theory of Light Absorption and Non-Radiative Transitions in F-Centres. *Proc. R. Soc. Lond. A. Math. Phys. Sci.* **1950**, *204* (1078), 406–423.

(24) Ridley, B. K. *Quantum Processes in Semiconductors*; Oxford Univ. Press, 1999.

(25) Bixon, M.; Jortner, J. Electron Transfer—from Isolated Molecules to Biomolecules. In *Advances in Chemical Physics*; 1999; pp 35–202.

(26) Lin, S. H.; Chang, C. H.; Liang, K. K.; Chang, R.; Shiu, Y. J.; Zhang, J. M.; Yang, T.-S.; Hayashi, M.; Hsu, F. C. Ultrafast Dynamics and Spectroscopy of Bacterial Photosynthetic Reaction Centers. In *Advances in Chemical Physics*; John Wiley & Sons, Inc.: New York, USA, 2002; pp 1–88.

(27) Krauss, T. D.; Wise, F. W. Coherent Acoustic Phonons in a Semiconductor Quantum Dot. *Phys. Rev. Lett.* **1997**, *79* (25), 5102–5105.

(28) Kelley, A. M. Exciton-Optical Phonon Coupling in II-VI Semiconductor Nanocrystals. *J. Chem. Phys.* **2019**, *151* (14), 140901.

(29) Kelley, A. M.; Dai, Q.; Jiang, Z. J.; Baker, J. A.; Kelley, D. F. Resonance Raman Spectra of Wurtzite and Zincblende CdSe Nanocrystals. *Chem. Phys.* **2013**, *422*, 272–276.

(30) Iaru, C. M.; Geuchies, J. J.; Koenraad, P. M.; Vanmaekelbergh, D.; Silov, A. Y. Strong Carrier–Phonon Coupling in Lead Halide Perovskite Nanocrystals. *ACS Nano* **2017**, *11* (11), 11024–11030.

(31) Besombes, L.; Kheng, K.; Marsal, L.; Mariette, H. Acoustic Phonon Broadening Mechanism in Single Quantum Dot Emission. *Phys. Rev. B* **2001**, *63* (15), 155307.

(32) Becker, M. A.; Scarpelli, L.; Nedelcu, G.; Rainò, G.; Masia, F.; Borri, P.; Stöferle, T.; Kovalenko, M. V; Langbein, W.; Mahrt, R. F. Long Exciton Dephasing Time and Coherent Phonon Coupling in CsPbBr 2 Cl Perovskite Nanocrystals. *Nano Lett.* **2018**, *18* (12), 7546–7551.

(33) Fu, M.; Tamarat, P.; Huang, H.; Even, J.; Rogach, A. L.; Lounis, B. Neutral and Charged Exciton Fine Structure in Single Lead Halide Perovskite Nanocrystals Revealed by Magneto-Optical Spectroscopy. *Nano Lett* **2017**, *17*, 27.

(34) Han, P.; Bester, G. Carrier Relaxation in Colloidal Nanocrystals: Bridging Large Electronic Energy Gaps by Low-Energy Vibrations. *Phys. Rev. B* **2015**, *91* (8), 085305.

(35)   Giustino, F. Electron-Phonon Interactions from First Principles. *Rev. Mod. Phys.* **2017**, *89* (1), 015003.

(36)   Kelley, A. M. Electron-Phonon Coupling in CdSe Nanocrystals. *J. Phys. Chem. Lett.* **2010**, *1* (9), 1296–1300.

(37)   Akkerman, Q. A.; Rainò, G.; Kovalenko, M. V; Manna, L. Genesis, Challenges and Opportunities for Colloidal Lead Halide Perovskite Nanocrystals. *Nat. Mater.* **2018**, *17* (5), 394–405.

(38)   Kilina, S. V.; Kilin, D. S.; Prezhdo, V. V.; Prezhdo, O. V. Theoretical Study of Electron–Phonon Relaxation in PbSe and CdSe Quantum Dots: Evidence for Phonon Memory. *J. Phys. Chem. C* **2011**, *115* (44), 21641–21651.

(39)   Liu, J.; Kilina, S. V.; Tretiak, S.; Prezhdo, O. V. Ligands Slow Down Pure-Dephasing in Semiconductor Quantum Dots. *ACS Nano* **2015**, *9* (9), 9106–9116.

(40)   Voznyy, O.; Mokkath, J. H.; Jain, A.; Sargent, E. H.; Schwingenschlögl, U. Computational Study of Magic-Size CdSe Clusters with Complementary Passivation by Carboxylic and Amine Ligands. *J. Phys. Chem. C* **2016**, *120* (18), 10015–10019.

(41)   Yazdani, N.; Nguyen-Thanh, T.; Yarema, M.; Lin, W. M. M.; Gao, R.; Yarema, O.; Bosak, A.; Wood, V. Measuring the Vibrational Density of States of Nanocrystal-Based Thin Films with Inelastic X-Ray Scattering. *J. Phys. Chem. Lett.* **2018**, *9* (7), 1561–1567.

(42)   Spoor, F. C. M.; Tomić, S.; Houtepen, A. J.; Siebbeles, L. D. A. Broadband Cooling Spectra of Hot Electrons and Holes in PbSe Quantum Dots. *ACS Nano* **2017**, *11* (6), 6286–6294.

(43) Spoor, F. C. M.; Kunneman, L. T.; Evers, W. H.; Renaud, N.; Grozema, F. C.; Houtepen, A. J.; Siebbeles, L. D. A. Hole Cooling Is Much Faster than Electron Cooling in PbSe Quantum Dots. *ACS Nano* **2016**, *10* (1), 695–703.

(44) Kamisaka, H.; Kilina, S. V.; Yamashita, K.; Prezhdo, O. V. Ultrafast Vibrationally-Induced Dephasing of Electronic Excitations in PbSe Quantum Dots. *Nano Lett.* **2006**, *6* (10), 2295–2300.

(45) Turyanska, L.; Patanè, A.; Henini, M.; Hennequin, B.; Thomas, N. R. Temperature Dependence of the Photoluminescence Emission from Thiol-Capped PbS Quantum Dots. *Appl. Phys. Lett.* **2007**, *90* (10), 101913.

(46) Houtepen, A. J.; Hens, Z.; Owen, J. S.; Infante, I. On the Origin of Surface Traps in Colloidal II–VI Semiconductor Nanocrystals. *Chem. Mater.* **2017**, *29* (2), 752–761.

(47) Giansante, C.; Infante, I. Surface Traps in Colloidal Quantum Dots: A Combined Experimental and Theoretical Perspective. *J. Phys. Chem. Lett.* **2017**, *8* (20), 5209–5215.

(48) Empedocles, S. A.; Bawendi, M. G. Quantum-Confined Stark Effect in Single CdSe Nanocrystallite Quantum Dots. *Science.* **1997**, *278* (5346), 2114–2117.

(49) Lin, C.; Gong, K.; F. Kelley, D.; Myers Kelley, A. Size-Dependent Exciton–Phonon Coupling in CdSe Nanocrystals through Resonance Raman Excitation Profile Analysis. *J. Phys. Chem. C* **2015**, *119* (13), 7491–7498.

(50) Empedocles, S. A.; Norris, D. J.; Bawendi, M. G. Photoluminescence Spectroscopy of Single CdSe Nanocrystallite Quantum Dots. *Phys. Rev. Lett.* **1996**, *77* (18), 3873–3876.

(51) Norris, D. J.; Efros, A. L.; Rosen, M.; Bawendi, M. G. Size Dependence of Exciton Fine Structure in CdSe Quantum Dots. *Phys. Rev. B* **1996**, *53* (24), 16347–16354.

(52) Dzhagan, V. M.; Lokteva, I.; Valakh, M. Y.; Raevska, O. E.; Kolny-Olesiak, J.; Zahn, D. R. T. Spectral Features above LO Phonon Frequency in Resonant Raman Scattering Spectra of Small CdSe Nanoparticles. *J. Appl. Phys.* **2009**, *106* (8), 084318.

(53) Mork, A. J.; Lee, E. M. Y.; Tisdale, W. A. Temperature Dependence of Acoustic Vibrations of CdSe and CdSe-CdS Core-Shell Nanocrystals Measured by Low-Frequency Raman Spectroscopy. *Phys. Chem. Chem. Phys.* **2016**, *18* (41), 28797–28801.

(54) Dzhagan, V. M.; Lokteva, I.; Valakh, M. Y.; Raevska, O. E.; Kolny-Olesiak, J.; Zahn, D. R. T. Spectral Features above LO Phonon Frequency in Resonant Raman Scattering Spectra of Small CdSe Nanoparticles. *J. Appl. Phys.* **2009**, *106* (8), 084318.

(55) Iaru, C. M.; Geuchies, J. J.; Koenraad, P. M.; Vanmaekelbergh, D.; Silov, A. Y. Strong Carrier–Phonon Coupling in Lead Halide Perovskite Nanocrystals. *ACS Nano* **2017**, *11* (11), 11024–11030.

(56) De Roo, J.; Ibáñez, M.; Geiregat, P.; Nedelcu, G.; Walravens, W.; Maes, J.; Martins, J. C.; Van Driessche, I.; Kovalenko, M. V.; Hens, Z.; et al. Highly Dynamic Ligand Binding and Light Absorption Coefficient of Cesium Lead Bromide Perovskite Nanocrystals. *ACS Nano* **2016**, *10* (2), 2071–2081.

(57) Krieg, F.; Ochsenbein, S. T.; Yakunin, S.; ten Brinck, S.; Aellen, P.; Süess, A.; Clerc, B.; Guggisberg, D.; Nazarenko, O.; Shynkarenko, Y.; et al. Colloidal CsPbX 3 (X = Cl, Br, I) Nanocrystals 2.0: Zwitterionic Capping Ligands for Improved Durability and Stability. *ACS*

Energy Lett. **2018**, *3* (3), 641–646.

(58)   Vandevondele, J.; Krack, M.; Mohamed, F.; Parrinello, M.; Chassaing, T.; Hutter, J. Quickstep: Fast and Accurate Density Functional Calculations Using a Mixed Gaussian and Plane Waves Approach. *Comput. Phys. Commun.* **2005**, *167* (2), 103–128.

(59)   Lippert, G.; Hutter, J.; Parrinello, M. A Hybrid Gaussian and Plane Wave Density Functional Scheme. *Mol. Phys.* **1997**, *92* (3), 477–488.

(60)   Hartwigsen, C.; Goedecker, S.; Hutter, J. Relativistic Separable Dual-Space Gaussian Pseudopotentials from H to Rn. *Phys. Rev. B* **1998**, *58* (7), 3641–3662.

(61)   Bussi, G.; Donadio, D.; Parrinello, M. Canonical Sampling through Velocity Rescaling. *J. Chem. Phys.* **2007**, *126* (1), 014101.